Chapter 4

Terahertz Fiber Sensing

Borwen You and Ja-Yu Lu

Additional information is available at the end of the chapter

http://dx.doi.org/10.5772/66345

Abstract

Terahertz fibers used for optical-sensing applications are introduced in this chapter, including the dielectric wires, ribbons and pipes. Different analyte conformations of the liquid, solid particle, thin film and vapor gas are successfully integrated with suitable fibers to perform high sensitivities. Based on the optimal sensitivities, analyte recognitions limited in traditional terahertz spectroscopy are experimentally demonstrated by the terahertz fiber sensors. Using the cladding index-dependent waveguide dispersion and high fractional cladding power of terahertz wire fiber, 20 ppm concentration between polyethylene and melamine particles can be distinguished. When the evanescent mode field of a terahertz ribbon fiber is controlled by a diffraction metal grating, subwavelength-confined surface terahertz waves potentially enable the near-field recognition for nano-thin films. Resonance waveguide field surrounding the terahertz pipe fiber is able to identify the macromolecule deposition in subwavelength-scaled thickness, approximately $\lambda/225$. For inner core-confined resonance waveguide field inside the terahertz pipe fiber, low physical density of the vaporized molecules around 1.6 nano-mole/mm^3 can also be discriminated.

Keywords: optical sensing, terahertz spectroscopy, terahertz optics

1. Introduction

Various dielectric fibers are introduced in this chapter for terahertz (THz) wave transmission and sensing. Most of THz-electromagnetic power guided along the proposed fiber is distributed in the air region, realizing long distance delivery of THz waves with low propagation loss and dispersion. The detection sensitivity consequently increases due to the sufficient field-analyte interaction length. Large portion of THz field evanescent in the air also makes the waveguide mode quite sensitive to the slight refractive index variation of the

analyte surrounding the fiber. The sensitive feature of THz refractive index is advantageous to minute material detection based on analyzing the propagation property change of waveguide mode. In this chapter, we address not only the waveguide characteristics and sensing mechanisms of the proposed THz fibers, but also the fiber-sensing schemes with the highest sensitivities, experimentally achieved via optimizing the waveguide geometric parameters. The introduced low-loss THz fibers are categorized based on their geometries including the wire-, ribbon- and pipe-fibers. The former two fibers have the subwavelength-scaled waveguide core and air cladding, allowing single mode transmission with loosely field confinement. The analytes distributed in the air cladding significantly influences the fiber dispersion of the waveguide modes. The pipe-fiber delivers and confines terahertz waves in the hollow air core based on the anti-resonant reflecting waveguide principle, leading to multiple resonant dips and exhibiting in the transmission spectrum. The analyte inducing slight variation of the optical path in the pipe wall or hollow core is able to significantly shift the resonant spectral dips. Such variation of waveguide dispersion or spectral shift for the proposed terahertz fibers are successfully measured by the fiber-based terahertz time domain spectroscopy to identify various minute analytes, such as subwavelength films, particles and volatile vapors.

2. Subwavelength plastic wire sensor

2.1. THz waveguide field along a plastic wire

The THz wire fiber has a circular cross section as the fiber core and an infinite air cladding, where the wire core size is smaller than the THz wavelengths and called as the subwavelength fiber [1]. The subwavelength fiber used to guide electromagnetic waves was first demonstrated in infrared frequency, performing a large portion of the evanescent power outside the fiber core [2]. On the basis of the evanescent waveguide field, the wire fiber is demonstrated to deliver THz wave in a long distance with very low waveguide loss. In this section, the polystyrene (PS) wire with a step refractive-index profile is taken as one example of a THz subwavelength fiber and its evanescent power in the air cladding is expressed in **Figure 1(a)**, which is calculated from the solutions of a general step-profile fiber [3]. The core diameter and THz refractive index of the PS core material are, respectively, 300 μm and 1.59 at 0.300 THz. **Figure 1(a)** shows the fractional THz power in the air cladding which is increased with wavelength and the guiding power at 3 mm-wavelength almost entirely expands outside the fiber core. Obviously, the power percentage of a waveguide mode in the air cladding exceeds 60% when the wavelength is longer than 1 mm. The large power ratio in the air cladding greatly reduces the THz-wave propagation loss along the wire. Three THz wavelengths, 0.75, 1.00 and 1.25 mm are observed for the relating across power distributions in radial (inset of **Figure 1(a)**) and their modal sizes based on the full width at half maximum (FWHM) are, respectively, 0.118, 0.438 and >6 mm. The waveguiding power obviously enhances near the core-cladding interface for the long wavelength waves. Such power enhancement is thus highly sensitive to detect analytes surrounding the wire core [3].

http://dx.doi.org/10.5772/66345

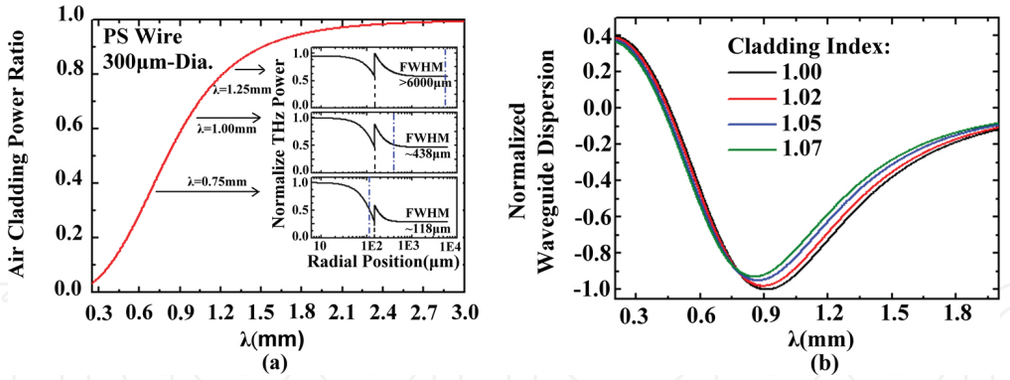

Figure 1. Calculation of the fiber-guiding THz-wave power ratio in the air cladding around a PS wire with a 300 μm core diameter. (Inset) THz-wave power distributes in the cross section of a PS wire, where the black dash line and blue dash dot line, respectively, indicate the wire radius, 150 μm and the HE_{11} modal size range at the full with of half maximum (FWHM) power. (b) Calculation results of PS wire waveguide dispersion, which are normalized with the air cladding index of 1.00 to observe the negative waveguide dispersion variation for cladding index increment up to 1.07 (Reprinted from Ref. [7] © 2009 OSA).

To assess the refractive index-sensing ability of the THz plastic wire fiber, the waveguide dispersion of a PS wire (300 μm core size) under various cladding indices are simulated (**Figure 1(b)**). The simulated results are normalized with respect to the lowest minimum value as "−1"for the negative waveguide dispersion in the waveguide dispersion spectrum. When the cladding refractive index is modified from 1.00 to 1.07, the waveguide dispersion dip becomes less negative and shifts toward a short wavelength [4]. The variation percentage of the waveguide dispersion dip, denoted as ΔD_{WG} is approximately proportional to the cladding index. For the case of a PS wire, ΔD_{WG} varies around 1% when 0.01 index increment at the fiber cladding is performed.

According to the theoretical results in **Figure 1(b)**, it reveals that the variation of waveguide dispersion dip is caused by the evanescent THz waves transmitted along different specimens with various refractive indices, where the air-cladding index is partially replaced by the analytes with higher refractive indices, i.e., >1.00. The plastic wire-sensing scheme is advantageous to guide long-wavelength THz waves within a narrow bandwidth because of the loose confinement and low transmission loss properties [5]. The fiber-sensing scheme, therefore, provides one possibility to use a simple THz spectral system avoiding strict spectrum criteria in the system, such as the broadband, high power or high frequency radiation. Advanced applications in remote sensing or the integration with lab-on-a chip probably becomes workable in THz frequency region by implementing this concept into practice.

2.2. Liquid-sensing results

Figure 2 schematically shows the optical configuration of a THz wire fiber-sensing scheme. THz radiation is emitted and detected by a pair of photoconductive switches, excited by a mode-locked pulse laser with a 100 fs pulse width, 80 MHz repetition rate and central wavelength of 800 nm. Two off-axis parabolic mirrors with effective focal length of 75 mm couple THz radiation from free space into the fiber. A 15-cm-long PS wire with a 300-μm-core

diameter is applied as a THz subwavelength fiber. After the 15-cm-long fiber propagation, the output THz waves are collimated by a lens and a pair of parabolic mirrors to couple the guided THz waves into a THz detector. The signal process of the measured THz waveform from the plastic wire waveguide follows the operation principle of THz time-domain spectroscopy, involving the amplitude and phase of an electric field oscillation [6].

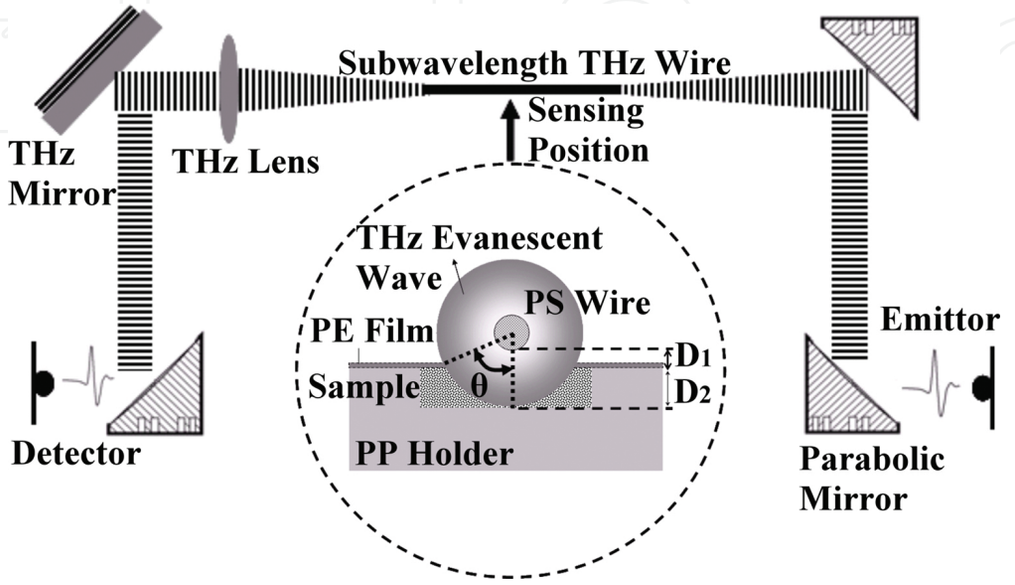

Figure 2. Optical configuration of a THz fiber system. (Inset) Geometric arrangement between the PS-wire-guided evanescent wave and the liquid sample holder (Reprinted from Ref. [7] © 2009 OSA).

We conduct the liquid-sensing experiment by integrating a sample holder, made of polypropylene (PP), beneath the PS wire for loading the liquid analyte. The PP holder contains two liquid channels with different lengths of 1 and 3 mm and the same width (6 mm) and depth (0.5 mm). A 10-μm-thick polyethylene (PE) film is covered on the top of liquid channels to prevent liquid evaporation under the ambient temperature and pressure. The waveguide dispersion can be derived from the phase difference of the transmitted THz waveform acquired from PS wire integrated with PP holder with and without the analytes loading.

The phase difference for THz wave transmitted along the wire with and without liquid samples is described as follows,

$$\Delta\phi \equiv \left(\phi_{sL1} - \phi_{airL1}\right) - \left(\phi_{sL2} - \phi_{airL2}\right) \tag{1}$$

where ϕ_{sL1} and ϕ_{airL1} represent the phases of THz waves pass through a L_1-long PP channel with and without a liquid analyte loading, respectively. Similarly, ϕ_{sL2} and ϕ_{airL2} refer to the phases of THz waves propagating through L_2-long PP channel with and without liquid analyte, respectively. The phase difference according to Eq. (1) is only contributed from THz wave along the $|L_1 - L_2|$ -long PS wire with the liquid analyte in the cladding region and the 2 mm-length (i.e., difference between 1- and 3-mm-long liquid channels) is specifically designed to sense

liquids with a sufficient signal-to-noise ratio to get the reliable phase difference. For other analytes with lower THz refractive index comparing to the liquid analyte, increasing the length difference of the two liquid channels is suggested. Based on the definition of a propagation constant, $\beta = |L_1 - L_2| \cdot \Delta\phi = 2\pi n_{eff}/\lambda$, the effective refractive index (n_{eff}) of the THz wavelength (λ) can be derived by substituting the measured $\Delta\phi$ in Eq. (2).

$$n_{eff} = \frac{\lambda \cdot \Delta\phi}{2\pi\left(L_2 - L_1\right)} + 1 \tag{2}$$

The measured waveguide dispersion (D_{WG}) along a PS wire with the sample cladding is then obtained from Eq. (3), relating to the group velocity (V_g) as formulated in Eq. (4). For different liquid samples loaded in the sensing scheme of **Figure 2**, the performed propagation constants (β) along the PS wire are certainly distinct to shift the feature of the negative waveguide dispersion curves, approximate to the calculation results of **Figure 1(b)**.

$$D_{wg} = \frac{d\left(V_g^{-1}\right)}{d\lambda} \tag{3}$$

$$V_g = -\frac{2\pi C}{\lambda^2} \cdot \frac{1}{d\beta / d\lambda} \tag{4}$$

On the basis of the geometric parameters of the wire radius (r), channel depth (D_2) and the separation between the wire and the liquid surface (D_1) as illustrated in the inset of **Figure 2**, the percentages of the waveguide mode spreading in the liquid and air space can approximately be estimated. Based on the spreading ratio of waveguide mode and effective medium concept, the theoretical effective refractive indices of waveguide mode relating the liquid samples can be estimated and the theoretical waveguide dispersion can consequently be calculated based on Eqs. (3) and (4). In experiment, the pure water and ethanol are employed as standard analytes to verify the fiber-sensing modality. The variation of waveguide dispersion at the spectral dip is successfully observed while the water and ethanol individually interact with the evanescent waves of the PS wire. The measured variation percentage of the waveguide dispersion dip well agrees to the theoretical calculation [7]. The result further reveals only the variation in the negative waveguide dispersion without the significant spectral shift as shown in **Figure 1(b)**.

Figure 3 shows the sensing result to recognize minute polymer powder grains dissolved in the ethanol, where the polymer powder grains are PE (434,272 ultra-high molecular weight, surface-modified polyethylene powder, Sigma–Aldrich Inc.) and melamine (Melamine, Nippon Bacterial Test Co., Ltd.) materials. A small amount of the both grains are mixed in ethanol solutions separately with various concentrations, 20–100 ppm (part per million, i.e.,

one milligram powder per one liter of ethanol in this case). The pure PE grains usually cannot be dissolved in ethanol; however, the used PE grains are modified as polar surfaces for a higher solubility in ethanol. In the ethanol solution, melamine powders are slightly solute and its solubility is larger than that of PE grains due to the polar molecular structure [8].

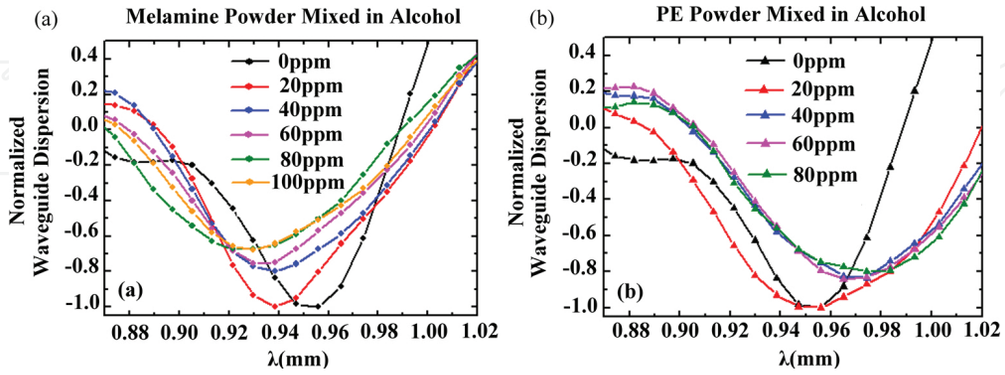

Figure 3. PS wire waveguide dispersions for liquid samples in the cladding, which are pure ethanol mixed with different concentrations of (a) melamine and (b) PE powders. It is normalized by the pure ethanol condition at the negative dispersion dip to observe their dispersion variation performance (Reprinted from Ref. [7] © 2009 OSA).

As illustrated in **Figure 3(a)**, apparent variation at waveguide dispersion dips is indeed observed while increasing the melamine concentration from 20 to 80 ppm in ethanol solutions. However, the variation of waveguide dispersion dips in the PE-ethanol solution occurred only when the PE concentration is altered from 20 to 40 ppm as shown in **Figure 3(b)**. Because the effective-cladding index of PS wire is changed with the solute concentration of analyte, the waveguide dispersion of THz waveguide mode is also modified and agrees with the theoretical prediction as shown in **Figure 1(b)**. Comparison between **Figure 3(a)** and **Figure 3(b)**, the waveguide dispersion dip variations (ΔD_{WG}) at the powder concentration of 40 ppm are 21 and 18%, respectively, for melamine- and PE-ethanol solutions. It implies more melamine grains can be dissolved in an ethanol solution, comparing to the PE grains. Such different dissolving abilities is reasonable because the polarity of melamine is higher than that of PE, which is easier to be dissolved by a polar liquid, ethanol.

3. Plastic ribbon fiber sensor

3.1. Subwavelength confinement using a metal grating integrated THz ribbon fiber

A subwavelength plastic ribbon has been demonstrated as a low-loss THz waveguide to deliver loosely confined THz waves with bandwidth of about 1 THz [9] for a long distance. Similar to the aforementioned plastic wire, the waveguide mode power of the ribbon fiber also mostly spreads in the air cladding. However, the ribbon fiber core is nonsymmetrical different from the circular core of a plastic wire and able to guide a broader bandwidth than that of a plastic wire. To excite the waveguide mode of the subwavelength ribbon fiber, the polarization

http://dx.doi.org/10.5772/66345

direction of the input THz waves should be parallel to the ribbon thickness, i.e., perpendicular to the thin-film surface.

Although the evanescent wave of a subwavelength fiber is highly sensitive to the refractive index variation in the air cladding, the much extensive modal field is not suitable to sense micro-particles or over layers in subwavelength scales. Subwavelength optics provides the schemes to visualize or sense those subwavelength-scaled analytes in the near-field region and the plasmonic waveguide [10] is one of the notable near-field sensors. To confine the evanescent waves along a THz ribbon fiber, the feasibility to increase the waveguide refractive index via integrating the ribbon fiber with a period metal structure is presented in this section. **Figure 4(a)** schematically depicts the hybrid THz plasmonic waveguide, constructed by one plastic ribbon and a 1D periodic metal grating. The diffraction metal grating has a length of 50 mm, a width of 15 mm and a thickness of *h*, machined on a brass sheet with a lattice constant of 1.5 mm and a slit width of 1 mm. It is attached on one side near the output end of the ribbon fiber. The ribbon fiber is made of a 20-μm-thick, 15-mm-wide and 22-cm-long PE plastic thin film.

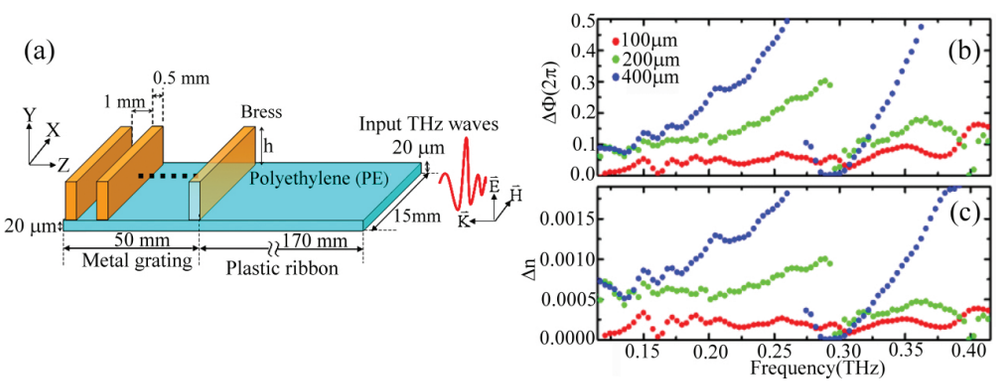

Figure 4. (a) Configuration drawing of the planar hybrid plasmonic waveguide. (b) Phase-variation spectrum contributed by different metal grating thicknesses. (c) Variation spectra about the effective waveguide refractive indices in different metal grating thicknesses (Reprinted from Ref. [13] © 2013 OSA).

Using a one-dimensional metal grating to generate and deliver THz spoof plasmons has been presented for the waveguide loss and dispersion properties [11]. The slit width and depth of a diffraction grating have a significant impact on the field confinement and propagation distance of the transverse magnetic (TM) polarized THz waves [12]. The ribbon fiber delivers TM waveguide mode, matching the polarization criterion of the THz spoof plasmons. As presented in **Figure 4(a)**, TM-polarized THz waves are edge-coupled to one end of the ribbon fiber from the free space, forming the weakly confined waveguide mode to propagate through a 170-mm-long fiber length. The stabilized waveguide mode would then directly enter a 50-mm-long integrated metal grating waveguide. When the loosely confined THz waves illuminate on the metal grating, partial transmission along grating periods occurs due to the mismatch in the cross-modal field and effective waveguide index. With the same slit width of 1 mm and grating period of 1.5 mm, we discuss the impact of various metal grating thicknesses, including 100, 200 and 400 μm, on the modal confinement of the propagated TM-wave.

The propagation vectors of the reflected and transmitted THz waves on the diffraction grating follows the momentum conservation relation as Eq. (5),

$$\bar{K}_{in} + \bar{K}_{\Lambda} = \bar{K}_{R} \tag{5}$$

where the vectors of K_{in}, K_R and K_Λ are, respectively, the propagation constants of the input and reflected THz waves along the ribbon fiber as well as a grating wave vector. The grating wave vector, K_Λ, equals $2\pi m/\Lambda$ where m and Λ are individually the Bragg diffraction order and the grating period. The directions of propagation constants, K_{in} and K_R, are opposite but have the same magnitude of $2\pi\nu n_{eff}/C$ for THz waves propagated along the integrated ribbon fiber, where ν, C and n_{eff} are, respectively, the THz wave frequency, speed of light in a vacuum and an effective waveguide refractive index. The diffraction grating works to reflect THz waves exactly at the Bragg frequencies in different orders, which can be derived as $mC/2n_{eff}\Lambda$ from Eq. (5). In the case of 1.5-mm-period metal grating, there are two narrow low-transmission bands found in experiment, caused by the Bragg reflections, respectively, at near 0.300 and 0.400 THz. Such spectral dip exactly at Bragg frequency is the result of phase-matching between the ribbon- and grating-waveguide modes. In experiment, the low order Bragg reflection dips, near the 0.100 and 0.200 THz, cannot be found because the large cross section of input THz wave leads to the low efficiency of coupling with the grating [13].

Figure 4(b) shows the measured results of the phase retardation ($\Delta\Phi$) of THz waves after the 50-mm-long propagation of the metal gratings with different thicknesses. The retarded THz wave phase is only considered from the metallic grating contribution because the PE ribbon fiber is normalized with the defined phase difference, $\Delta\Phi = \Phi_G - \Phi_{Blank}$, where Φ_G and Φ_{Blank} are, respectively, THz-wave phases of the electric-field oscillation passing the 220-mm-long ribbon fiber with and without the 50-mm-long metal grating. Equation (6) expresses refractive-index variations (Δn) relating to the phase difference ($\Delta\Phi$).

$$\Delta n = C\Delta\phi \Big/ (2\pi\upsilon L) \tag{6}$$

The light speed in vacuum, THz wave frequency and the length of a metal grating are, respectively, denoted as C, ν and L in Eq. (6). The refractive index increment resulted from the metal gratings with different thicknesses is therefore illustrated in **Figure 4(c)** based on **Figure 4(b)** and Eq. (6). The results show 100-μm-thick grating slightly performs the phase retardation of the guided THz waves, which is much smaller than those of the 200- and 400-μm-thick gratings. When the grating thickness increases to 200-μm thickness, zero phase difference occurs at 0.300 and 0.400 THz, representing the phase-matching condition, i.e., $\Phi_{Blank} = \Phi_G$, between the ribbon guided THz waveguide mode (K_{in}) and the reflected surface plasmonic (SP) modes of the hybrid waveguide (K_R) via the metal grating (K_Λ) structure. For those ribbon-guided THz waves with the zero phase difference, their power can be completely transferred to the spoof surface plasmon polaritions (SPP)modes and reflected through the Bragg reflection,

http://dx.doi.org/10.5772/66345

corresponding to the zero-refractive index variation for index matching between the two modes (**Figure 4(c)**).

The effective waveguide modal indices along the metal grating are obviously larger than those of a blank ribbon waveguide and proportional with the frequency increment within the deliverable frequency range. The waveguide theory expresses the high waveguide refractive index is able to confine the extended EM fields close to the waveguide core as a small spatial mode [14]. The metal grating delivering THz waves approximate to the modal field of a dielectric waveguide. It is found the 400-μm-thick grating performs the largest phase difference and effective waveguide index within 0.300–0.360 THz and <0.260 THz because of the largest across section to interact input THz waves. More closely confined THz SPPs can therefore be guided along the 400-μm-thick grating, instead of the 200- and 100-μm-thick gratings.

Figure 5(a) shows the measured and simulated decay lengths on one side of the bare ribbon and hybrid grating waveguides with different grating thicknesses. The waveguide decay lengths with and without metal grating decrease as the frequency increment of THz waves. The minimum decay length of the blank ribbon is around 0.56 mm at frequencies beyond 0.300 THz. However, the decay length is apparently extended for THz frequency below 0.350 THz while the ribbon-guided waves input the 100-μm-thick metal grating. Contrarily, the decay lengths shrink above the 200- and 400-μm-thick metal gratings for THz frequencies, respectively, approaching the 0.300 and 0.250 THz. The trend about these decay lengths can also be obtained in FDTD calculation.

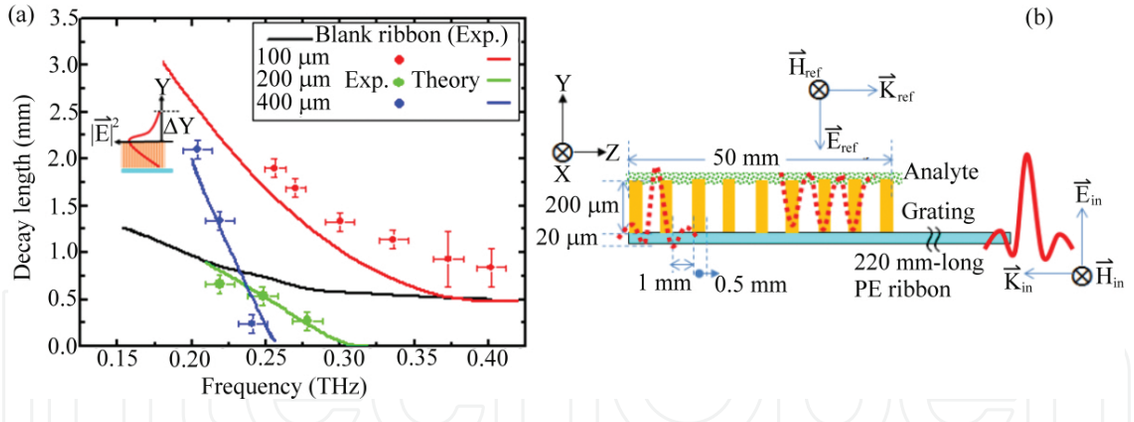

Figure 5. (a) Measured and calculated decay lengths of the guiding THz waves along a blank ribbon and different integrated gratings with 100, 200 and 400 μm thicknesses (Reprinted from Ref. [13] © 2013 OSA). (b) Sensing configuration of a plastic ribbon fiber integrated with a metal grating (Reprinted from Opt. Express 21, 21087–21096 (2013). © 2013 OSA).

3.2. Particle sensing using a hybrid THz waveguide

In a traditional THz spectroscopy, to recognize solid particles with size much smaller than THz wavelength, the required analyte amount should be sufficient to form tablets and the thickness should be precise in order to obtain the correct THz information. For minute material detection, a versatile and flexible THz-sensing platform is necessary. This section in-

troduces the particle-sensing methodology using the metal-grating-integrated hybrid THz waveguide and assesses its detection ability. The sensing scheme is schematically plotted in **Figure 5(b)**, where the particle analyte is located on a dielectric substrate which is attached on the metal grating of the hybrid waveguide. The particle loaded membrane substrate is entirely covered above the metal grating, becoming one part of the hybrid plasmonic waveguide and to facilitate passing through the subwavelength confined THz surface plasmonic waves (SPWs). The evanescent fields of the THz-SPWs interact with the particle analyte in a sufficiently long distance, leading to the enhanced THz response in spectrum. Due to the multiple reflections from the metal grating at Bragg frequencies, the optical paths of THz waves in the hybrid waveguide are obviously longer than those on the bare ribbon. The long optical path makes the guided THz-SPWs quite sensitive to any slight variation of dielectric analytes located within the evanescent field range of waveguide mode. The propagation constants of the resonant waves are equal to $2\pi n_{eff}\nu/C$, where n_{eff}, ν and C denote the effective refractive index, resonant frequency of the THz-SPWs and light speed in vacuum, respectively. For a specific grating period Λ and an incident angle, the resonant frequency of a THz-SPW is inversely proportional to the effective refractive index of the hybrid plasmonic waveguide (n_{eff}).The change of the effective refractive index related to surrounded analyte would thereby change the resonant dip in THz transmission spectrum, providing a straightforward spectral feature for the sensing application.

To conceptually demonstrate the minute particle-sensing capability using the hybrid waveguide sensor, a chemical compound of Bi_2CuISe_3 with irregular grain shapes and nonuniform particle sizes, <300 μm, is considered as a sample under test in the experiment. Different amounts of compound analyte are prepared to produce distinct effective indices of the THz-SPW propagated on the hybrid waveguide for sensitivity test. A 60-μm thick, 50-mm-long and 15-mm-wide PE film was used as a sample substrate and attached to the grating surface to adhere the analyte (Bi_2CuISe_3) in different quantities (e.g., 16.5, 29.3 and 55.3 μmole). The analytes with different amounts are individually loaded on the PE substrate to be sensed by the SPWs and the fourth-order resonance dip can be found performing evident spectral shifts (**Figure 6(a)**). For the blank PE-film substrate and sample loading amounts of 16.5, 29.3 and 55.3 μmole, the transmission dips are, respectively, at 0.276, 0.266, 0.259 and 0.237 THz. Obvious spectral shift can be found because of the granular particles contributing the high material dispersion in THz frequency as illustrated in the inset of **Figure 6(a)**.

Figure 6(b) summarizes the resonant dip-shifts of THz-SPWs that relate to waveguide-index variations obtained from different thicknesses of blank PE substrates and different quantities of chemical compounds on a 60 μm-thick substrate. For different thicknesses of the blank PE substrates, their spectral responses are resulted from the distinct waveguide index variation, ranging from 0.2 to 0.467, because of their different substrate thicknesses. A fitting curve (black line in **Figure 6(b)**) is presented as a quadratic function. The detection sensitivity of the hybrid plasmonic waveguide can be considered as the tangential slope of each data point, defined as the frequency-shift range per refractive index unit, i.e., $\Delta\nu/\Delta n$. Using different PE substrate thicknesses in the sensing scheme, the estimated sensitivities based on 20, 50 and 90 μm thicknesses are, respectively, 261, 197 and 159 GHz/RIU. The particle-sens-

http://dx.doi.org/10.5772/66345

ing ability using a 60 μm thick PE film as substrate shows the spectral shift is almost linearly proportional to the waveguide index variation (Δn) within Δn range of 0.395–0.626, as indicated by the red fitting line in **Figure 6(b)**. Based on the slope of the linear fitting curve (red line), the sensitivity is estimated as 163 GHz/RIU which is less than the sensitivity of the 60 μm thick thin film (~187 GHz/RIU acquired from the slope of the quadratic fitting curve in **Figure 6(b)**). Therefore, a uniform overlayer can be more easily detected than a powder analyte based on the waveguide-sensing scheme even though the granular material has considerably high THz-wave dispersion.

The sensing performance of the hybrid THz plasmonic waveguide dependent on the polynomial fits in **Figure 6(b)** is then discussed on the sample substrate of a 20 μm thick PE film, whose sensitivity is about 261 GHz/RIU. Its thin-film detection ability approaches to 1.8 μm when the thin film index is 1.50 and the spectral resolution is down to 0.004 THz. The optical path difference (OPD) is approximately 2.7 μm and the thickness resolution can approach $\lambda/289$ of the 4th-order resonance wave at 0.380 THz. For sensing the powder on the substrate of a 60 μm thick PE film (163 GHz/RIU), the minimal detectable molecular quantity is approximately 13 μmole on the 15 mm-wide and 50 mm-long substrate area, corresponding to the molecular density of 17.3 nano-mole/mm^2. When the spectral resolution is further decreased to 1 GHz, 454 nm-thick thin film (681 nm-OPD) could be resolved in the resonance spectral shift. Therefore, the hybrid waveguide-sensing scheme is certainly compatible with the planar terahertz metamaterial [15] to act as a sensitive thin film sensor in THz frequency for nano-thin film detection. Metal hole array and planar terahertz metamaterials are difficult to sense nonuniform and random distributed particles, even though the highest sensitivity of metal hole array approaches 2 THz/RIU [16]. In the hybrid waveguide-sensing scheme, the particles layer can be considered as an effective waveguide cladding of the hybrid plasmonic waveguide sensor to induce the waveguide index change from various particle quantities.

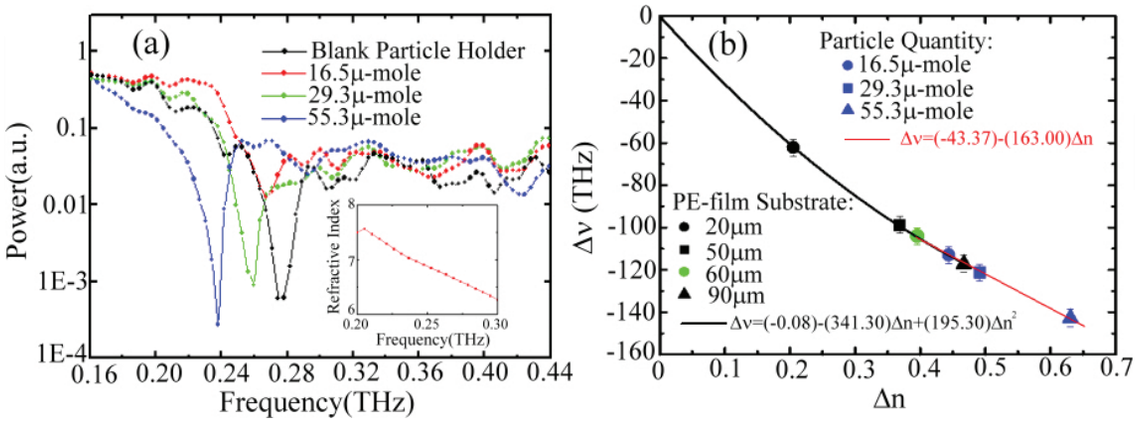

Figure 6. (a) Waveguide transmission spectra for different amounts of powder analytes loaded on a PE film substrate; (inset) THz refractive index spectrum of a tablet-formed compound Bi_2CuISe_3; (b) relation between effective waveguide refractive index variation (Δn)and the spectral shift range ($\Delta\nu$) of the fourth-order SPW resonance, which is compared with the blank grating condition (Reprinted from Opt. Express 21, 21087–21096 (2013). © 2013 OSA).

4. Dielectric pipe fiber sensor

4.1. Overlayer-sensing principle

A THz pipe fiber is a hollow tube which is composed of a ring-shaped dielectric cladding and an air-core; it has been demonstrated as a broadband and low-loss THz waveguide [17]. The dielectric ring cladding, inherently served as a Fabry-Pérot resonator, can transmit THz waves in the hollow core based on anti-resonant reflecting optical waveguide principle (ARROW) [18] to form multiple transmission peaks in a transmission spectrum, called as antiresonant modes. The resonant modes of the ring-shaped Fabry-Pérot resonator leak out of the ring cladding and form dips in a transmission spectrum [19]. The spectral dip position of a resonant mode is closely related to the thickness and refractive index of the ring-shaped cladding. A thin film attaching to the ring waveguide cladding is able to change the resonant condition of the THz pipe fiber and results in resonant-frequency-dip shift [20]. Sensing the tiny variation in refractive index or thickness of an adsorbed molecular film near the ring cladding is therefore applicable.

A double-layered Fabry-Pérot model is proposed to calculate the resonant mode of the THz pipe fiber with a composite cladding [21], where the effective thickness of the sample or the cladding is defined as Eq. (7),

$$\tau_{cld\ or\ fim} = d_{cld\ or\ fim}\sqrt{n^2_{cld\ or\ fim} - n^2_0}, \tag{7}$$

where the $d_{cld\ or\ fim}$ and $n_{cld\ or\ fim}$ are the physical thickness and the refractive index of pipe wall or thin-film analyte, respectively. A calibration experiment is conducted by attaching different thicknesses of PE films on the ring-shaped pipe wall to estimate the sensitivity for thin-film detection. It is found that the sensitivity of thin-film detection is proportional to THz resonance wavelength, where long THz resonance wavelengths are equivalent to the low-order resonant modes of the pipe fiber based on the fundamental of ARROW waveguide. For thin-film-sensing application by the THz-pipe fiber, the low order resonant mode with long wavelength is thus able to perform high sensitivities for those analyte thicknesses down to subwavelength scales. The calibration results also show the pipe with a thin pipe wall has a higher sensitivity, comparing to the thick pipe wall made of the same material. We take into account the effects of pipe-wall thickness, index and THz resonance wavelength on sensing capability and the thin-film detection sensitivity (S_λ) can be deduced in Eq. (8), where τ_{cld} and τ_{fim} are defined in Eq. (7).

$$S_\lambda = \frac{\lambda_m}{\tau_{cld} + \tau_{fim}}. \tag{8}$$

From Eq. (8), approaching highly sensitive THz pipe-fiber sensor can be described as following two conditions. One way is that the effective thickness of a pipe cladding (τ_{cld}) should be small

when the dip shift is observed at a specific resonant wavelength (λ_m) for a certain thickness of the thin-film analyte (τ_{fim}). The other way is the low-order resonant modes, i.e., long resonance wavelengths, λ_m, are suggested to be employed under the geometry of a pipe sensor for sensing analyte. More evanescent power is surrounded the ring cladding for the lower-order resonant modes to perform the higher sensitivity, comparing to the shorter resonant wavelengths. For a low index or a small physical thickness of pipe-wall, a resonant THz wave will be loosely confined in the waveguide cladding and results in more THz evanescent power surrounding the pipe-wall for efficient interaction with the analyte thin films near the waveguide cladding.

Based on the result of the calibration experiment, a PP tube with the highest sensitivity is used to probe the macro-molecular overlayer adhered on the pipe inner-wall. The PP pipe fiber used to sense the macro-molecular layer has a length of 15 cm, a cladding (i.e., pipe wall) thickness of 0.29 mm and an inner-core diameter of 12 mm. Different thicknesses of the macro-molecular overlayers are prepared by dissolving different amounts of carboxypolymethylene powders, named as carbopol 940 (Boai Nky Pharmaceuticals Ltd.), in water with different weight-concentrations, including 1, 2, 3 and 4%. The Carbopol 940 powder belongs to macromolecular material with molecular weight about 104,000 g per mole, corresponding to 1450 monomer units [22]. The carbopol liquids have high viscosity, adhering to the inner pipe wall and forming macro-molecular layers via gravity-driven flowing and natural evaporation.

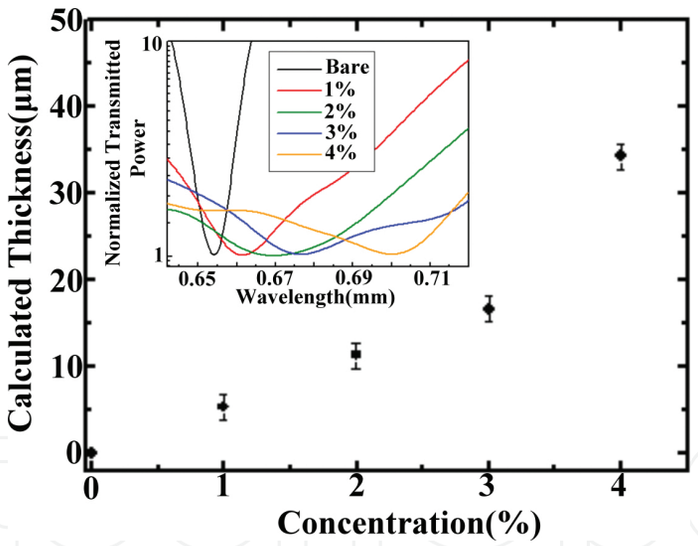

Figure 7. Estimated thicknesses of carbopol micro-molecular layers for different concentrations of the carbopol solutions. (Inset) The transmission spectra of the first resonant mode along a 0.29-mm-thick pipe-wall PP tube, loaded with various thicknesses of the macro-molecular layers (Reprinted from Ref. [21] © 2010 OSA).

The waveguide spectral features in **Figure 7** show different macro-molecular layers with different physical thicknesses can be detected from the spectral shift of resonance waveguide modes. The 1st resonance mode wavelength is at 0.654 mm and shifted toward the long wavelength range when increasing the concentrations of carbopol aqueous solutions. The spectral shift of the resonant dip is owing to the different thickness of macro-molecular layer adhered on the PP cladding and the distinct thickness of molecular over layer is formed by

different viscosities of carbopol solutions [18]. The wavelength spectral positions (λ_m) of the resonant dips are 0.661, 0.669, 0.676 and 0.700 mm, respectively, for 1, 2, 3 and 4%- carbopol aqueous solutions. The thicknesses of the carbopol molecular layer can thus be estimated through the double-layered Fabry-Pérot models illustrated in **Figure 7**, where the THz refractive index of the carbopol-layer is around 1.2. In Eq. (9), the resonance wavelength, physical thicknesses and refractive indices of PP-pipe wall, macromolecular layer and the inner core refractive index are, respectively, denoted as λ_m, d_1, n_1, d_2, n_2 and n_0.

$$\lambda_m = \frac{2\left(d_1\sqrt{n_1^2 - n_0^2} + d_2\sqrt{n_2^2 - n_0^2}\right)}{m} \tag{9}$$

The estimation shows the thicknesses of carbopol-molecular layers are around 5.3, 11.3, 16.7 and 34.3 μm, respectively, for the 1-, 2-, 3- and 4%- solutions. The minimum detectable thin film thickness of the PP-tube-sensing scheme can therefore be estimated with the sensitivity of 0.0030 mm/μm and the system spectral resolution, ~0.0057 mm. Taking a carbopol-layer as an example, the detectable thickness increment can be down to 2.9 μm (~λ/225), corresponding to the resolution of carbopol molecule quantities as low as 1.22 picomole/mm^2. However, molecular resolution limited in the spectral dip shift would be resulted from the broadened bandwidth at the resonance wavelength, which is observed in the inset of **Figure 7**. The interference theory explains the same intensity of interfered waves performs high visibility [23], but the case of carbopol-layer has obvious THz waves absorption to decay the interference visibility with broadening resonance bandwidth.

4.2. Vapor-sensing principle

The THz pipe fiber can provide a sharp spectral line-width of resonant mode with a large portion of evanescent field spreads outside the pipe cladding, facilitating to integrate with various biochips for highly sensitive molecular sensing. Such evanescent wave characteristic is difficult to achieve in the metallic cavity type bio-sensors despite they possess the ultrahigh quality factor (or Q-factor) for sensing applications [20]. In addition, the pipe fibers are easy to commercially acquired without any complex fabrication. Based on above advantages, the dielectric-pipe-fiber-based refractive index sensor could potentially be applied in micro-fluidic systems for bio-chemical detection and inspecting industrial pollutants. Many industrial and environmental pollutants are toxic gases and harmful to animals. This section further introduces the capability to identify various vapors using the resonant modes of pipe fiber. To demonstrate vapor sensing, a pipe made of glass material is taken as the sensing fiber to prevent the volatile analytes from eroding/damaging the pipe-wall. In the vapor-sensing experiment, a small amount of different volatile liquid droplets is individually injected into the glass pipe and completely evaporate into vaporized molecules in the sealed hollow core under normal ambient condition. The transmitted THz waves and the vaporized analytes are simultaneously confined in the same channel to provide a sufficient interaction length and result in sensitive detection of minute vapors.

http://dx.doi.org/10.5772/66345

According to Eq. (10), the resonant dip wavelength (λ_m) changes with inner core refractive index (n_{cor}), and various vapors in the hollow core can thus be identified by detecting the spectral shift of a certain resonant dip (m).

$$\lambda_m = \frac{2d\sqrt{n_{cld}^2 - n_{cor}^2}}{m},\ m = 1, 2, 3\ldots \tag{10}$$

To realize a highly sensitive detection of vaporized analyte in the hollow core, the resonant waves in the pipe wall must be sufficiently evanescent toward the hollow core because the sufficient interaction is required. Based on the transverse power distributions of resonant waves in a pipe waveguide [24], the higher THz transmission power in the hollow core is observed in the higher-order resonant-dip, i.e., the dips in the high frequency range. **Figure 8(a)** shows the vapor-sensing example based on a 30 cm-long glass pipe, possessing the inner core diameter and the pipe-wall thickness are, respectively, 5.57 and 1.17 mm. The vapor inducing dip-frequency-shift only occurs in a resonance dip of 0.452 THz and other resonance dips in the low-frequency range do not exhibit any spectral shift. It does not follow the simulated results in **Figure 8(b)** because the leaky power of the low-order resonance-wave in the hollow core is insufficient to sense the vapor molecules. It also practically presents the evanescent field strength of a pipe resonant modes within the inner core is critical for the vapor sensing.

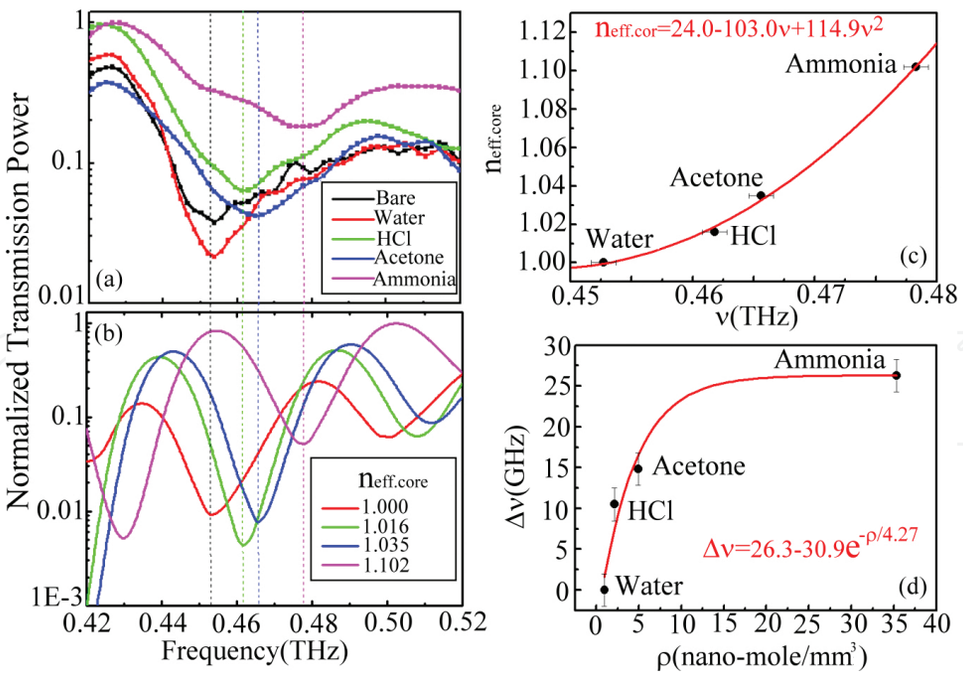

Figure 8. (a) Spectral dip shift of the glass-pipe resonance wave at 0.452 THz for sensing different volatile liquids. (b) Theoretical estimation of the inner core refractive indices to match the related spectral dip positions for the vapor-sensing results. (c) The spectral relation of the inner core refractive indices for different vapors. (d) Relation between the spectral dip shift and the related molecular densities (Reprinted from Ref. [24] © 2012 OSA).

The vapors are prepared by dropping 0.05 cm^3 liquids individually of water, hydrochloric acid (HCl), acetone and ammonia inside the hollow core of glass pipe with vapor pressure saturation. The sensing result shows the spectral dip at 0.452 THz can be shifted with different levels (**Figure 8(a)**), locating at 0.461, 0.465 and 0.477 THz, respectively, for the hydrochloric acid, acetone and ammonia vapors. Trying to match the spectral dip position, the effective inner core refractive indices can be calculated by FDTD method (**Figure 8(b)**), which are 1.016, 1.035 and 1.102, respectively, for the vapors of hydrochloric acid, acetone and ammonia. The relation is then summarized in **Figure 8(c)** between the spectral dip frequencies and the effective core-indices of the glass-pipe fiber, which is filled with different vapors. Those inner core refractive indices are distinct due to the different vapors even though the same liquid volume is inserted inside the pipe hollow core. The relation between the effective inner core refractive index and resonance frequency in **Figure 8(c)** can be fit with one polynomial to evaluate any slight index variation inside the pipe hollow core. For the example of water sample, the relating spectral dip is consistent with and without inserting the vapor because of the considerably low density, comparing to those volatile liquids. It means the effective inner core index of water case approximates to 1.0.

Different volatile liquids have individual vapor pressures at normal atmospheric pressure and temperature. There are different quantities of vaporized molecules in the same hollow core volume. Vapor pressures of volatile liquids are proportional to the quantities of vaporized molecules in the same chamber. High vapor molecule density in the hollow core eventually results in the higher effective core-index than the air core, performing apparent blue shift at the resonant spectral dip at 0.452 THz. When we consider the vapor pressures in literatures for water, hydrochloric acid, acetone and ammonia at 1 atmosphere and 20°C, their saturated vapor pressures are, respectively, around 17 mm-Hg [25], 38 mm-Hg [26], 202 mm-Hg [26] and 308 mm-Hg [25]. Thereby, the effective core-index is proportional to the increase of the sample vapor pressure. When the vaporized molecular density is estimated on the basis of the ideal gases, the corresponding densities are illustrated in **Figure 8(d)**. The relation is fit with one nonlinear curve, representing the blue shift level would cease approaching the value of 10 nano-mole/mm^3. The minimum detectable molecular quantity would be approximately 7.8 micromole in the glass pipe, corresponding to a molecular density of 1.6 nano-mole/mm^3 when the system spectral resolution is about 4 GHz.

5. Conclusion

In this chapter, THz fiber sensors are successfully demonstrated in a PS-plastic wire, a PE-plastic ribbon integrated with a metal grating, a PP- and glass pipes. The presented fiber sensors are highly sensitive to the existence and variation of minute molecules and enable sensing analytes with different formations, including the liquids, powder grains, vapor gases, thin films and overlayers. A subwavelength plastic wire fiber has large percentages of evanescent field surrounding the fiber cores and there is negative waveguide dispersion sensitive to the refractive index variation in the air cladding. Fluidic channel is successfully integrated to detect minute concentration of melamine grains dissolved in the ethanol solutions

ranged from 20 to 80 ppm. A plastic ribbon fiber also has the extended evanescent waveguide modes, but it is further advantageous to integrate a metal grating becoming a hybrid plasmonic waveguide based on the optical properties of a THz ribbon fiber, including the TM polarized wave guidance and the broadband transmission. When the optimal overlapping between the metal grating and ribbon waveguide modes, subwavelength confined surface waves can be excited and used for sensing powder grains or thin-film analytes. When the spectral resolution of THz system is reduced down to 1 GHz, the nano-scaled OPD detection could be realized by the plastic ribbon fiber sensor. The dielectric pipe fiber with a hollow air core is also considered as one important THz fiber sensor because of the built-in resonator along the pipe wall. To achieve highly sensitive detection, the applicable resonant modes for thin-film and vapor detections are absolutely different because of the different cross locations of the target analytes. Using the pipe fiber to adsorb liquids with high viscosities as one thin film layer on the inner pipe wall, the low frequency resonance modes or small pipe wall thicknesses are required to achieve the best sensitivity due to the much extended evanescent resonance field. For sensing the inserted vapors at the pipe hollow core, the sensitive THz waves contribute at the high order resonant modes because their resonant field well confined at the inner core efficiently interacting the vapors. In the sensing experiments, the detectable overlayer thickness and vaporized molecular density via THz pipe fiber sensors can be reduced to 2.9μm (~λ/225)and 1.6 nano-mole/mm^3, respectively.

Author details

Borwen You[1] and Ja-Yu Lu[2*]

*Address all correspondence to: jayu@mail.ncku.edu.tw

1 Division of Applied Physics, Faculty of Pure and Applied Sciences, University of Tsukuba, Tsukuba, Japan

2 Department of Photonics, National Cheng-Kung University, Tainan, Taiwan

References

[1] L. J. Chen, H. W. Chen, T. F. Kao, J. Y. Lu and C. K. Sun. Low-loss subwavelength plastic fiber for terahertz waveguiding. Opt. Lett. 2006;31:308–310.

[2] L. Tong, R. R Gattass, J. B Ashcom, S. He, J. Lou, M. Shen, I. Maxwell and E. Mazur. Subwavelength-diameter silica wires for low-loss optical wave guiding. Nature. 2003;426:816–819.

[3] J. Lou, L. Tong and Z. Ye. Modeling of silica nanowires for optical sensing. Opt. Express. 2005;13:2135–2140.

[4] L. Tong, J. Lou and E. Mazur. Single-mode guiding properties of subwavelength-diameter silica and silicon wire waveguides. Opt. Express. 2004;12:1025–1035.

[5] H. W. Chen, Y. T. Li and C. L. Pan, J. L. Kuo, J. Y. Lu, L. J. Chen and C. K. Sun. Investigation on spectral loss characteristics of subwavelength terahertz fibers. Opt. Lett. 2007;32:1017–1019.

[6] B. Ferguson and X. C. Zhang. Materials for terahertz science and technology. Nat. Mater. 2002;1:26–33.

[7] B. You, T. A. Liu, J. L. Peng, C. L. Pan and J. Y. Lu. A terahertz plastic wire based evanescent field sensor for high sensitivity liquid detection. Opt. Express. 2009;17:20675–20683.

[8] R. E. N. Baozeng, L. I. Chen, Y. U. A. N. Xiaoliang and W. A. N. G. Fu'an. Determination and correlation of melamine solubility. Chin. J. Chem. Eng. 2003;54:1001–1003.

[9] C. Yeh, F. Shimabukuro and P. H. Siegel. Low-loss terahertz ribbon waveguides. Appl. Opt. 2005;44:5937–5946.

[10] W. L. Barnes, A. Dereux and T. W. Ebbesen. Surface plasmon subwavelength optics. Nature. 2003;424:824–830.

[11] L. Shen, X. Chen and T. J. Yang. Terahertz surface plasmon polaritons on periodically corrugated metal surfaces. Opt. Express. 2008;16:3326–3333.

[12] S. A. Maier, S. R. Andrews, L. M. Moreno and F. J. G. Vidal. Terahertz surface plasmon-polariton propagation and focusing on periodically corrugated metal wires. Phys. Rev. Lett. 2006;97:176805.

[13] B. You, J. Y. Lu, W. L. Chang, C. P. Yu, T. A. Liu and J. L. Peng. Subwavelength confined terahertz waves on planar waveguides using metallic gratings. Opt. Express. 2013;21:6009–6019.

[14] C. R. Williams, S. R. Andrews, S. A. Maier, A. I. F. Dominguez, L. M. Moreno and F. J. G. Vidal. Highly confined guiding of terahertz surface plasmon polaritons on structured metal surfaces. Nat. Photonics. 2008;2:175–179.

[15] J. F. O'Hara, R. Singh, I. Brener, E. Smirnova, J. Han, A. J. Taylor and W. Zhang. Thin-film sensing with planar terahertz metamaterials: sensitivity and limitations. Opt. Express. 2008;16:1786–1795.

[16] G. Liu, M. He, Z. Tian, J. Li and J. Liu. Terahertz surface plasmon sensor for distinguishing gasolines. Appl. Opt. 2013;52:5695–5700.

[17] C. H. Lai, Y. C. Hsueh, H. W. Chen, Y. J. Huang, H. C. Chang and C. K. Sun. Low-index terahertz pipe waveguides. Opt. Lett. 2009;34:3457–3459.

[18] N. M. Litchinitser, A. K. Abeeluck, C. Headley and B. J. Eggleton. Antiresonant reflecting photonic crystal optical waveguides. Opt. Lett. 2002;27:1592–1594.

[19] C.-H. Lai, B. You, J.-Y. Lu, T.-A. Liu, J.-L. Peng, C.-K. Sun and H. C. Chang. Modal characteristics of antiresonant reflecting pipe waveguides for terahertz waveguiding. Opt. Express. 2010;18:309–322.

[20] A. M. Zheltikov. Ray-optic analysis of the (bio)sensing ability of ring-cladding hollow waveguides. Appl. Optics. 2008;47:474–479.

[21] B. You, J. Y. Lu, J. H. Liou, C. P. Yu, H. Z. Chen, T. A. Liu and J. L. Peng. Subwavelength film sensing based on terahertz anti-resonant reflecting hollow waveguides. Opt. Express. 2010;18:19353–19360.

[22] J. O. Carnal and M. S. Naser. The use of dilute solution viscometry to characterize the network properties of carbopol microgels. Colloid Polym. Sci. 1992;270:183–193.

[23] N. Kinrot. Analysis of bulk material sensing using a periodically segmented waveguide Mach–Zehnder Interferometer for biosensing. J. Lightwave Technol. 2004;22:2296–2301.

[24] B. You, J. Y. Lu, C. P. Yu, T. A. Liu and J. L. Peng. Terahertz refractive index sensors using dielectric pipe waveguides. Opt. Express. 2012;20:5858–5866.

[25] Chap. 5. In: J. A. Dean, editor. Lange's handbook of chemistry. McGraw-Hill; 1999.

[26] E. W. Washburn, editor. International critical tables of numerical data, physics, chemistry and technology, volume IV. Knovel; 2003.

IntechOpen